# Design and characterization of a tunable amplifier for 500 - 1000 kHz frequency range

Master's thesis, 25.11.2022

Author:

Aukusti Jurvanen

Supervisors:

Tommi Eronen, Risto Kronholm

UNIVERSITY OF JYVÄSKYLÄ
DEPARTMENT OF PHYSICS

# Tiivistelmä

Jurvanen, Aukusti
Pro Gradu-tutkielma
Fysiikan laitos, Jyväskylän yliopisto, 2022, 56 sivua

Tässä työssä suunniteltiin, simuloitiin ja rakennettiin radiotaajuus (RF) -vahvistin toimimaan säädettävällä taajuusalueella. Vahvistimella saadaan tuotettua korkeajännitteisiä radiotaajuussignaaleja ionikimputtimelle, jolla parannetaan tutkimuksissa käytettävän ionisuihkun laatua. Työn tavoitteena oli rakentaa vahvistin, jolla saadaan tuotettua 400 $V_{pp}$ jännitesignaali ionikimputtimen elektrodeille ja joka operoi 500 kHz - 1000 kHz taajuusalueella. Lopulta 600 kHz - 1000 kHz taajuusalue saatiin katettua halutulla 400 $V_{pp}$ jännitteen amplitudilla.

Avainsanat: RF-vahvistin, ionikimputin, resonanssipiiri

# Abstract

Jurvanen, Aukusti
Master's thesis
Department of Physics, University of Jyväskylä, 2022, 56 pages.

In this work, an RF amplifier was designed, simulated and constructed to operate in an adjustable frequency range. The amplifier produces high voltage radio frequency signals that radiofrequency quadrupole (RFQ) cooler-buncher uses for improving the quality of an ion beam. The goal of the thesis was to build an amplifier that can deliver an output voltage up to 400 $V_{pp}$ to the cooler-buncher electrodes with a frequency range between 500 kHz and 1000 kHz. The frequency range of 600 kHz - 1000 kHz was finally covered with a wanted 400 $V_{pp}$ output amplitude.

Keywords: RF-amplifier, cooler-buncher, resonant circuit

# Contents

# 1 Introduction

## 1.1 Motivation

In the accelerator laboratory of the University of Jyväskylä (JYFL-ACCLAB) the radioactive ions are produced for the experimental studies of the nuclear structure and fundamental interactions, for example. The radioactive ion beam needs to be shaped to such form that the ions can be used for measurements. An ion beam cooler-buncher consisting of a radiofrequency quadrupole (RFQ) trap is an essential part of the IGISOL facility in the accelerator laboratory. The cooler-buncher is used for cooling down the ion beams and confining the ions to the central axis of the device [1]. This results in a better quality ions and enables the forming of ion bunches to be used in further studies.

The RFQ cooler-buncher requires static and alternating electric fields to operate properly, i.e. to allow proper ion confinement in the device. For this, the RF signal is required to be typically up to 400 volts peak-to-peak ($V_{pp}$) of amplitude and up to 1000 kHz of frequency, or even more while satisfying the Mathieu parameters for ion motion stability [2]. Such a field requires an amplifier that amplifies the input RF signal of wanted frequency from function generators, which can typically provide output signal only up to 10 $V_{pp}$.

The ions of different masses and charges, specifically their mass-over-charge ratio, $m/q$ (typically, studied ion range from 50 u/e to 180 u/e), require different RF frequencies and voltages inside the cooler-buncher for optimal control and efficiency. Therefore, the RF amplifier should be adjustable by both frequency and amplitude to operate efficiently. The objective of this thesis was to design, simulate and construct a new RF amplifier for the cooler-buncher that is adjustable in frequency range between 500 kHz and 1000 kHz and delivers the output voltage up to 400 $V_{pp}$. This enables the better quality and controlling of ion beam for a wider $m/q$ range of nuclei than before.

## 1.2 IGISOL facility

In the Accelerator laboratory of the University of Jyväskylä the ion-guide isotope-separator on-line (IGISOL) facility seen in Figure 1 utilizes the ion guide technique, where the nuclear reaction products are stopped and thermalized in flowing (helium) gas [3]. The technique was developed in the 1980's to produce exotic radioactive beams of ions for further measurements. The exotic ions can be used to the study, for example nuclear astrophysics [4], neutrino physics [5], fundamental interactions and nuclear structure [6] [7] through, for example, atomic mass spectroscopy, laser spectroscopy and decay spectroscopy. The IGISOL technique has a fast ion extraction time (below 100 ms) [8] and is chemically intensitive [3] which makes it possible to produce a wide range of nuclei for the studies.

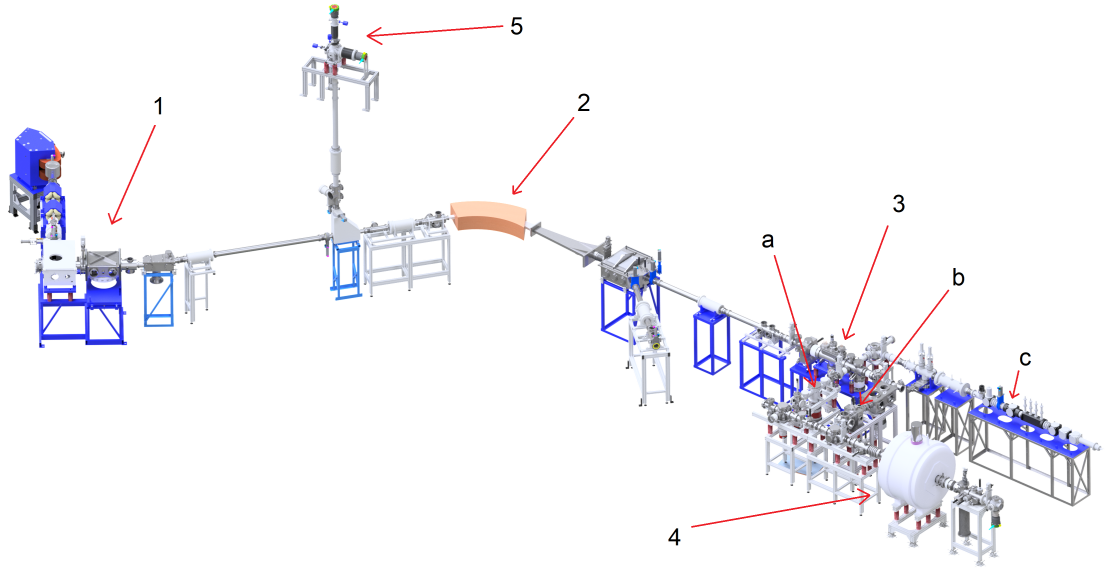


**Figure 1.** The IGISOL facility at the university of Jyväskylä. With a collision between accelerated beam and the production target (1), the desired reaction products are formed. The ions are thermalized and extracted as a 30-kV ion beam and then directed through the dipole magnet (2), which acts as a coarse mass separator. From there, ions are transferred into radio-frequency quadrupole (RFQ) cooler-buncher (3) where they are cooled down, confined radially and collected into bunches. The ion bunches are then extracted to further studies, for example into the JYFLTRAP Penning trap for mass measurements (4). The offline ion source station (5) is marked as well as other experimental setups: multi-reflection time-of-flight mass spectrometer (a), high resolution laser resonance ionization setup RAPTOR (b) and collinear laser spectroscopy (c). Figure from [9], modified.

The ions for the studies are created by directing an ion beam from a particle accelerator to the reaction target of selected material. The most commonly used reaction is fission, which is initiated on natural uranium with 20 - 30 MeV protons. The reaction products are formed in the target and recoil out of the target material while losing energy in collisions with the target and additional stopping material. The remaining recoil energy of the ions is reduced with the collisions with the helium gas [8]. Only the ions that get stopped in the gas are able to exit the gas cell as an ion beam. The most energetic reaction products are lost in the collisions with the walls of the device while the least energetic products have not enough energy to exit the target into the gas volume. Most of the surviving reaction products remain as singly charged ions, which exit the gas cell volume through a small nozzle and are accelerated with a voltage of 30 kV so that the ions can be transported further.

Immediately after the target area the ions are directed through a dipole magnet, which is used as a coarse mass separator resulting in all ions having the same mass number to pass. The mass-separated ions are guided further into a cooler-buncher where they are cooled down and collected into bunches [8]. The formed ion bunches are then extracted from the cooler-buncher and directed to further studies, for example to the collinear laserspectroscopy line, multi-reflection time-of-flight (MR-TOF) mass spectrometer or to the JYFLTRAP Penning trap mass spectrometer for better mass separation or mass spectrometry. The RFQ cooler-buncher is an essential part of the beam line since with the bunched ion beams the efficiency of the latter devices can be improved. In autumn 2022 there were 5 different experimental setups that require cooled and bunched beams: MR-TOF, [10], JYFLTRAP [8], RAPTOR [11], Collinear laser spectroscopy [12] and MORA [13].

## 1.3 RFQ cooler-buncher

The radiofrequency quadrupole (RFQ) cooler-buncher cooles down the ions by means of confining the ions spatially and by letting the ions thermalize with helium gas. The confinement of the ions in the device is achieved with the use of alternating RF electric fields. The frequency range of the electric fields is typically from 100 kHz to 10 MHz. Ions can also be accumulated in a potential well and then extracted from the device in bunches. The collisions of the ions with the low pressure buffer gas (usually helium) inside the cooler-buncher cools down the ions as well as reduces their radial motion around the optical axis. [14]. The cooler-buncher operates more

efficiently with higher amplitudes and frequencies of the RF signal which enables the higher amount of charge to be stored in RFQ and increases the transfer efficiency of the device [14].

The coordinate system used in this thesis is illustrated in figure 2. The axis parallel to the electrodes of the cooler-buncher is called the optical axis (z-axis in figure 2). The radial position perpendicular to the optical axis is on the xy-plane.

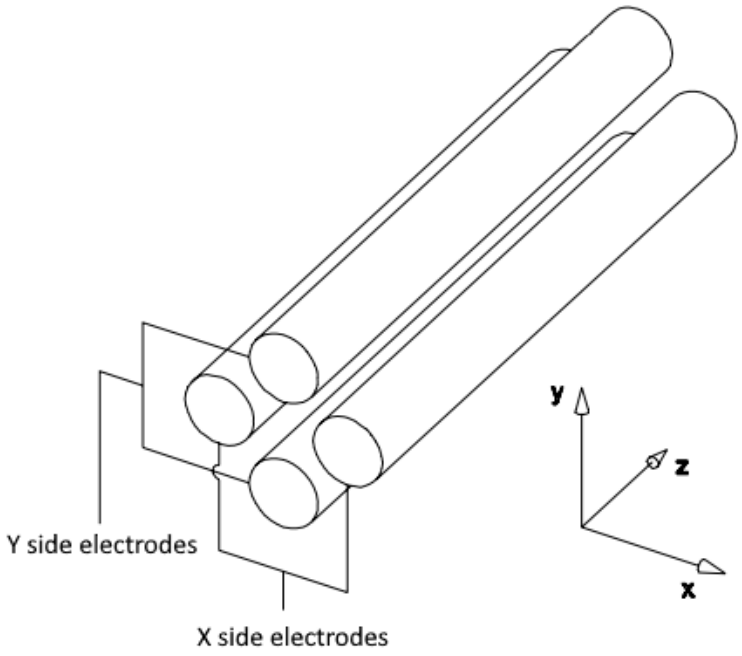


**Figure 2.** Configuration of the RF electrodes of a cooler-buncher. The RF signals in x-side electrodes are in the same phase together but in the opposite phase related to the y-side electrodes. This alternating RF electric field forms the radial saddle potential on the xy-plane of the cooler-buncher as seen in figure 3. Figure from [2], modified.

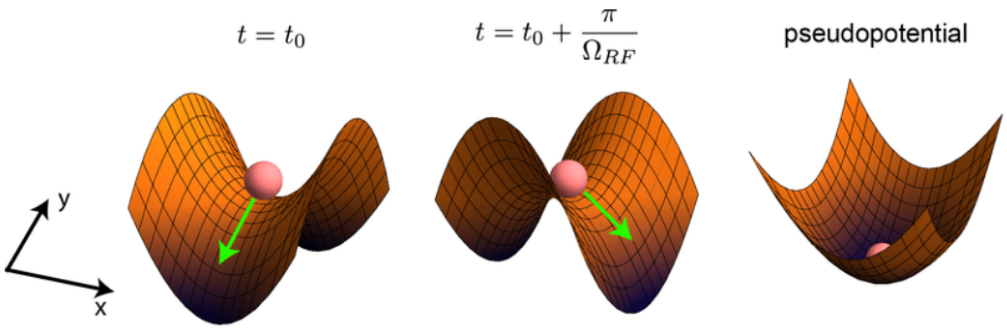


**Figure 3.** By applying the alternating RF signal on the x- and y-side electrodes in the opposite phases one can generate the saddle potential for the ions on the xy-plane. By choosing the appropriate Mathieu parameters $a$ and $q$ presented in section 1.3.1 the ions with different masses and charges can be defined on the axis along the cooler-buncher. These parameters set the suitable values for the amplitude and frequency of the RF signal as seen from equations (2). Figure from [15], modified.

### 1.3.1 Ion motion inside the RFQ

The motion of a single ion inside the cooler-buncher can be written in the form of so called Mathieu equations for both $x$ and $y$ directions of the radial movement [16]

$$\begin{aligned} \frac{d^2x}{d\tau^2} + (a - 2q\cos 2\tau)x = 0, \\ \frac{d^2y}{d\tau^2} + (a - 2q\cos 2\tau)y = 0 \end{aligned} \tag{1}$$

where $a$ and $q$ are the Mathieu parameters related to the particle properties, RFQ geometry and the applied electric fields. They can be further presented as

$$\begin{aligned} a = \frac{8QU}{mr_0^2\omega^2} \\ \text{and} \\ q = \frac{4QV}{mr_0^2\omega^2}, \end{aligned} \tag{2}$$

where $m$ and $Q$ are the mass and the charge of the ion, $U$ is the DC quadrupole component and $V$ and $\omega$ are the amplitude and angular frequency of the RF signal,

respectively. The dimensionless time parameter $\tau$ is defined as $\tau = \frac{\omega t}{2}$ and $r_0 = 10$ mm is the characteristic dimension of the cooler-buncher and defined as half of the distance between opposite side electrodes [2].

The equations of motion (1) are stable in both x- and y-directions only in a few regions of combinations of Mathieu parameters $a$ and $q$. One stable region is shown in figure 4. There are also other stable regions but only the closest to the origin is usually used in experiments [17]. This region of the combinations of the Mathieu parameters gives restrictions for the cooler-buncher RF amplitudes and frequencies as seen in equation (2). For this work, the design frequency range for the amplified RF signal was set from 500 kHz to 1000 kHz, requiring the peak-to-peak amplitude to be 400 $V_{pp}$.

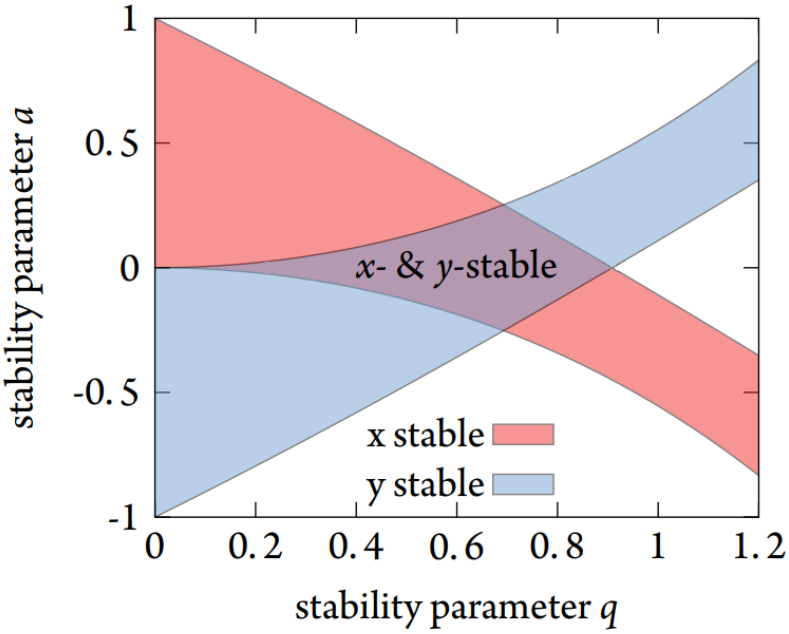


**Figure 4.** The stable region of the radial movements for both x- and y-directions for the single ion as a function of Mathieu parameters $a$ and $q$. There are also other stable regions but usually only this one closest to the origin is used for the experiments [17]. Figure from [17], modified

The radial spread of the ions coming into the cooler-buncher is reduced inside the cooler-buncher via collisions with the atoms of a buffer gas. These interactions with the gas cause ions to radially disperse from the optical axis of the cooler-buncher while the ions thermalize with the gas. This dispersion is countered with an RF field [14]. The gas collision combined with the RF field results in ions cooling to the axis

of the device.

In addition to the RF signal confining the ions radially also a decreasing DC potential is superimposed on top of the RF to form a decreasing potential towards the other end of the device. This DC potential is applied into 16 segments [2] into which the electrodes are divided. The combined signal of RF and DC confines the ions not just radially on the z-axis but pushes them also towards the potential well at the far end of the device. This potential well is produced by applying an increased DC potential to the end plates of the cooler-buncher to prevent ions from escaping from the device. After the ions are stabilized in the potential well they can be extracted from the cooler-buncher by switching the end plate potential lower than the potential of the last electrode. This principle is shown in figure 5.

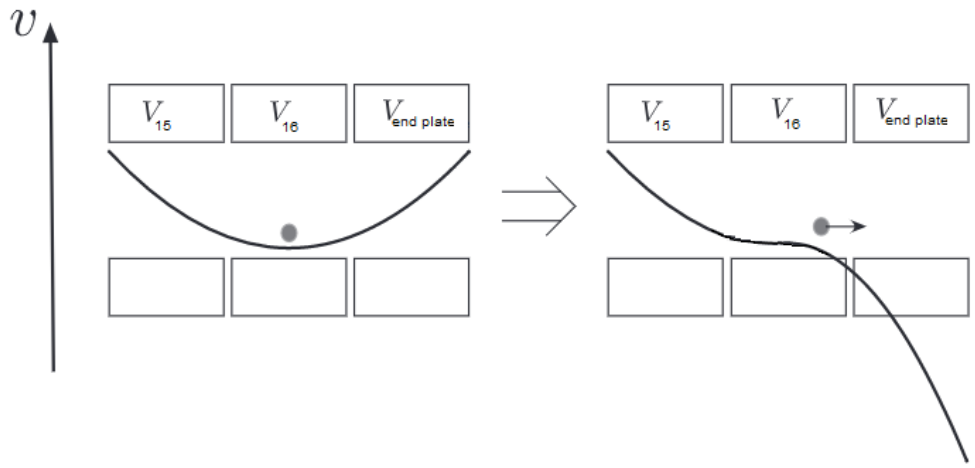


**Figure 5.** After the ions are stabilized in the cooler-buncher they can be extracted from the device by lowering the DC potential of the end plates. This forces the bunched ions out of the cooler-buncher. Figure from [14], modified.

### 1.3.2 Cooler-buncher configuration

Ideally, the electrodes of the cooler-buncher would be hyperboloids extending to infinity in order to have a perfect quadrupolar potential. A realistic quadrupole needs to use truncated hyperboloids or even cylindrical rods, which forms a reasonable precise quadrupolar potential when the radius of the rod ($\rho$) and the distance of the surface of the rods from the center ($r_0$) has ratio [18]

$$\frac{\rho}{r_0} = 1.14511. \tag{3}$$

In the main section of the RFQ cooler-buncher the cylindrical electrode rods are 40 cm of length and have radius $\rho = 11.5$ mm. They are located $R = 10$ mm away from the optical axis [2]. The rods are each divided into 16 segments onto which the decreasing DC potential mentioned in section 1.3.1 is applied. The configuration of the main section is seen in figures 6 and 7. Both ends of the main section are enclosed with DC-only plates that have narrow aperture for ions to pass and to minimize flow of the helium gas. The aperture in the extraction side plate enables the ions to be transported into first out of the two so-called bunching sections of the device, which are located right after the main section of the cooler-buncher. They are separated from the main section and from each other by DC plates. Voltages on these plates can be switched to allow transferring of the accumulated ions into the first bunching section and similarly to the second bunching section with lower gas pressure. After eventual cooling, the ions are extracted from the cooler-buncher through the aperture in the final end plate by lowering its potential significantly. This principle is illustrated in figure 6. The two bunching sections of the cooler-buncher enable the simultaneous accumulation and extraction of the ions which increases the efficiency of the cooler-buncher.

The RF signals for the cooler-buncher electrodes mentioned in section 1.3.1 are generated by waveform generators (Keysight 33500B), which can be set to output signal of wanted frequency. However, the output amplitude of the generators is only 10 $V_{pp}$ into 50 Ω load. This means that the RF signal needs to be amplified to the 400 $V_{pp}$ before attaching it to the cooler-buncher electrodes. This is done with the RF amplifier which amplifies the signals from generators for both x- and y-sides of the electrodes. The amplifier also needs to be able to amplify signals of different frequencies as mentioned in section 1.1. The operation of the amplifier is based on

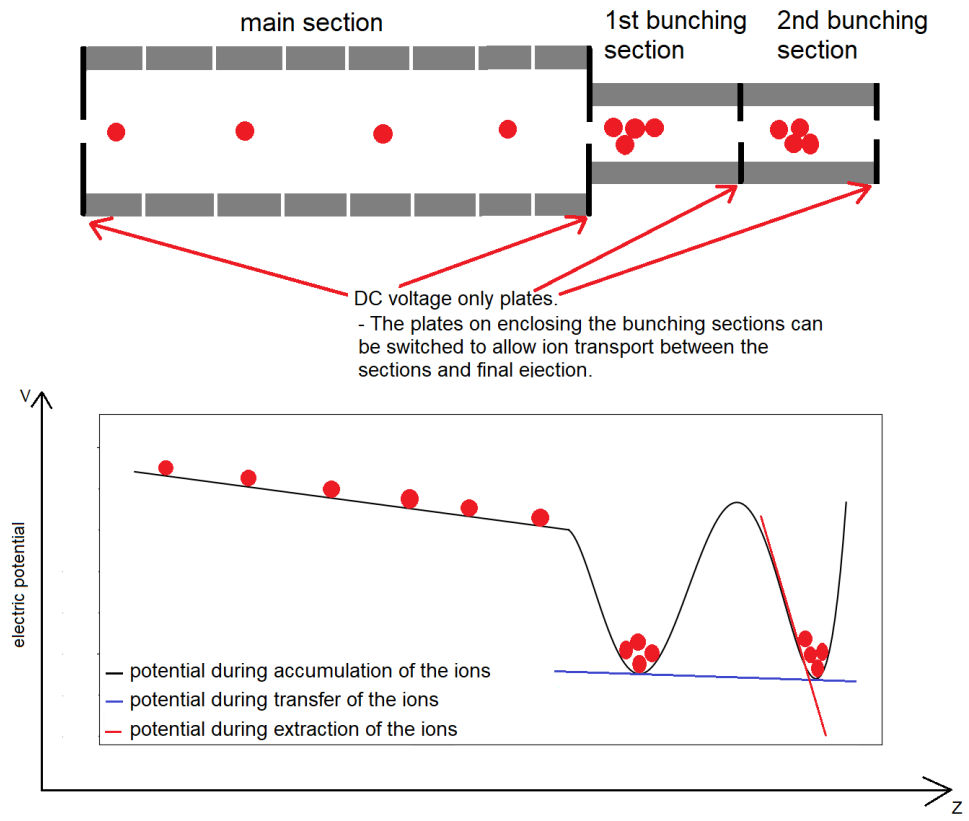


**Figure 6.** Configuration and electrical potential of the cooler-buncher during the transfer of the ions. First the ions are accumulated into the first bunching section by the descending potential through the main RFQ section. The accumulated ion bunches are transferred to the second bunching section by lowering the voltage in the plates between the sections. By changing the voltage of the final end plate the cooled ion bunches are extracted from the cooler-buncher to the further studies. The DC voltage of the plates can be tuned between -100 V and +100 V.

the transformer ramping up the voltage and a frequency-adjustable resonant circuit to change the resonant frequency for the amplifier.


**Figure 7.** The configuration of the RFQ main section. The nearly cylindrical rods are seen on the front and the connections for the each segment of the electrodes are seen on the left. The device is 40 cm of length and divided into 16 segments for application of the decreasing axial DC potential.

# 2 Theoretical background

The goal of this thesis work was to design an RF amplifier capable of producing the desired RF signals described earlier in section 1.3.1. The working principle of the amplifier is based on the resonant LC circuit which is described in the following section. Also, the use of RF amplifiers in other research facilities is handled.

## 2.1 Resonant frequency and $Q$ factor of an LC circuit

LC circuit is an electrical circuit where an inductor with inductance $L$ and a capacitor with capacitance $C$ form a closed loop. An LC circuit consisting only of inductance $L$ and capacitance $C$ is an idealized model which assumes no dissipation of energy due to resistance $R$ of the circuit. In practical applications there is always some amount of resistance in the circuit within the components and connecting wires.

Operation of the LC circuit is based on the energy oscillating back and forth between the components of the circuit. The inductor stores the energy in its magnetic field, when the electric current flows through the wiring while the capacitor stores the energy in its electric field, depending on the voltage across the plates. The voltage of the capacitor will drive a current through the inductor which induces a magnetic field in the inductor. This magnetic field will then cause the current flow in the opposite direction of the circuit resulting in the capacitor to be charged again. In an ideal LC circuit this cycling will continue endlessly. With any $R$ present, the energy is slowly dissipated into heat.

The significant feature of the LC circuit is its resonance, which occurs at the specific frequency, depending on the inductance and capacitance values of the components. At the resonant frequency the inductive and capacitive reactances of the circuit are of equal magnitude

$$2\pi f L = \frac{1}{2\pi f C} \tag{4}$$

from which one can solve the resonance frequency to be

$$f_r = \frac{1}{2\pi\sqrt{LC}}. \tag{5}$$

If the LC circuit is driven at its resonant frequency, a small input signal can excite a large output voltage. This is used as a working principle of the RF amplifier mentioned before in section 1.3.2.

In the amplifier, a ferrite core transformer is used to ramp up the RF signal amplitude. A ferrite core material offers low Eddy current losses when alternating magnetic field is applied into the core material. The secondary LC circuit consists of the capacitance of the electrodes and the chosen inductance of the transformer coil. In addition, adjustable capacitors are used in the LC circuit to adjust the resonance of the circuit to the desired frequency.

The maximum amplitude of the RF signal is achieved when the LC circuit is at the resonant frequency [19]. When the LC circuit is driven off-resonance, a lot of energy is dissipated in the system, including in the ferrite core of the transformer. The heating of the core material changes its relative permeability leading to a inductance shifting and thus the achieved amplitude is reduced[20]. To keep up the amplitude, additional power is required to the primary side of the circuit because of this power loss caused by heating. The reachable amplitude is limited by the available RF power in the primary side.

One can see from equation (5) that changing the inductance or the capacitance of the circuit changes its resonant frequency. A change of the resonant frequency is needed because ions of different masses and charges require different frequencies and amplitudes inside the cooler-buncher as mentioned in section 1.3.1 and the LC circuit needs to stay in the resonance as mentioned before. In this work, the inductance of the circuit was decided to be kept constant and changing the resonant frequency of the LC circuit was done by changing the capacitance of the circuit which is explained further in section 3.3.

The resonance in the LC circuit can be quantified by so called quality factor $Q$ which is defined as a ratio of energy stored to the energy dissipated during each cycle in the circuit. It can be shown that the quality factor of the circuit is dependent on the resonant frequency and corresponding bandwidth by the expression [19]

$$Q = \frac{\text{resonant frequency}}{\text{bandwith}}. \tag{6}$$

The $Q$ factor is seen as the narrowness of the voltage peak of the circuit at resonance. The higher $Q$ factor of the circuit results in larger peak amplitudes of the voltage but also makes the resonant frequency range of the circuit narrower and the LC circuit more sensitive to tune to a specific frequency. The $Q$ factors of the LC circuit are the main result in this thesis and they are calculated in section 4.

## 2.2 RF amplifiers used in research facilities

RF amplifiers are widely used in different research facilities mainly as a part of ion traps and ion guide designs, see for example [21], [22]. Commonly, the amplifier designs follow the same working principle: a primary driver circuit that can provide high power but limited amplitude and a secondary LC circuit connected to the actual load electrodes so that $L$ of the circuit is chosen so that required frequency is obtained and high enough amplitude is provided. Each amplifier has its own operating areas as a function of frequency and amplitude, which is determined by the component values in the circuit. Also the core material and the winding of the transformer is an important factor of the circuit characterization.

At the Institut für Angewandte Physik in Frankfurt, an RF amplifier with 3.5 MHz of frequency has been used with a ferrite core and a resonant circuit [23] where the MEQALAC accelerator in the USA uses a custom RF amplifier by Airity technologies. This delivers a high output signal up to 1.4 $kV_{pp}$ with the frequency range from 12 MHz to 15 MHz [24]. In Darmstadt, at the FAIR, the frequency range from 310 kHz to 560 kHz with the amplitude of 20 $kV_{pp}$ is achieved with Thales TH555 amplifers [25]. At the LPC Caen in France, the frequency range of the RF signal from 1 kHz to 220 MHz is delivered through home-built amplifier. The amplifier consists of a transformer wired around a ferrite core material and variable capacitor which can change the resonant frequency of the circuit [26].

# 3 Amplifier Construction

This section describes the structure of the amplifier as well as the construction of its components. The amplifier circuit consists of two major parts: the primary (driver) and the secondary (resonant) circuits. The primary side consists of an RF driver circuitry, which provides low amplitude but high power RF signal. The secondary side consists of a resonant circuit including the electrodes of the RFQ where finally the high-amplitude RF signal is needed. Before the RFQ electrodes the amplified RF signal is coupled with the DC voltage as described in section 1.3.1. This is done with the RF-DC box into which the RF signal is driven through a 100 nF capacitor. There is also a 100 nF capacitor in the output for each of the cooler-buncher electrode segments. The DC voltage is brought to the electrode segments through 2.2 mH inductors which protects the DC circuits from high voltage RF signals. By changing the capacitance of the secondary circuit using additional parallel-connected tunable capacitors, one can change the resonant frequency of the circuit and thus the frequency in the cooler-buncher, see section 2.1. The two sides are coupled through a transformer, which defines the amplification factor of the amplitude for the secondary side. The schematics of the circuit is shown in figure 8. A separate amplifier circuit is needed for both x- and y-side electrodes of the cooler-buncher. That is why two similar amplifier circuits are constructed.

## 3.1 Driver amplifiers

As seen from figure 8 the first step in the circuit after the function generator is the operational amplifier. In this project, ADA4870 [27] was selected as the driver amplifier. ADA4870 is an unity gain stable feedback amplifier which provides a stable voltage gain of 4.5 for up to 40 $V_{pp}$ of amplitude [28]. The amplitude of the output signal from the function generator (Keysight 33500B, [29]) is 10 $V_{pp}$ at the maximum so the amplification with ADA4870 to the maximum of 40 $V_{pp}$ of amplitude with a frequency range between 500 kHz and 1000 kHz can be tuned.

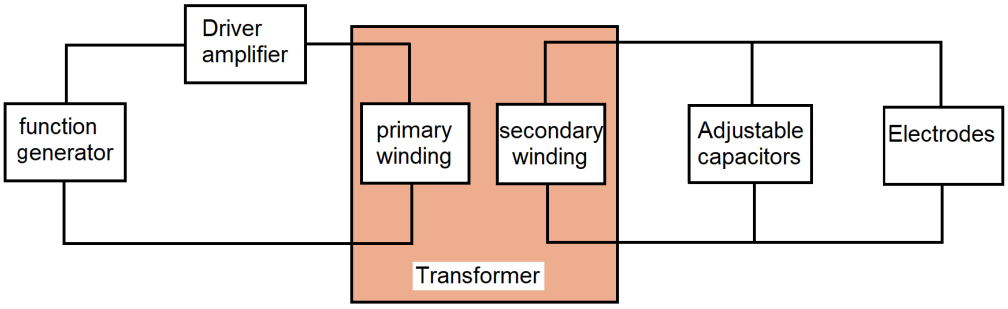


**Figure 8.** Schematic of the amplifier. The RF signal from function generator is amplified with a driver amplifier and delivered to the primary side of the transformer. The secondary side of the transformer and the capacitors form the secondary side of the circuit. The amplified signal is delivered to the electrodes of the cooler-buncher.

### 3.1.1 Cooling the operational amplifier

When driving ADA4870 with parameters close to its maximum values so that it outputs full power, it can generate up to 10 W of heat [27]. Without proper cooling it will be damaged in a few seconds. The cooling was realized by attaching ADA4870 onto a heat sink. The quality of a heat sink is measured with a unit called thermal resistance. It describes the ability of the heat sink to resist flow of thermal energy. The thermal resistance is represented with a unit of °C/W, indicating the temperature rise per unit rate of heat dissipation. Thus, a heat sink with smaller thermal resistance value will cool down the operational amplifiers more efficiently.

The operational temperature range of the ADA4870 amplifier is from -40 °C to +85 °C [28]. The total power dissipation in the amplifier is the sum of the power dissipated in the output stage plus the quiescent power. When considering the maximum of 10 W of power dissipation one can calculate the needed thermal resistance of the heat sink from equation [28].

$$\theta_{HS} = \left(\frac{T_J - T_A}{P_{DISS}}\right) - (\theta_{JC} + \theta_{CBOT} + \theta_{TIM}), \tag{7}$$

where $T_J$ is the maximum junction temperature (150 °C) [27], $T_A$ is the ambient temperature, $P_{DISS}$ is the chip power dissipation, $\theta_{JC}$ is the chip thermal resistance, $\theta_{CBOT}$ is the thermal resistance of the chip solder material and the PCB and $\theta_{TIM}$ is the thermal resistance of TIM(thermal interface material). The thermal resistance values are obtained from ADA4870 user guide [28]. With these values the upper

limit for the thermal resistance of a heat sink is

$$\begin{aligned} \theta_{HS} &= \left(\frac{150-85}{10}\right) - (1.1+1.0+0.3) \\ &= 4.1°\text{C/W} \end{aligned} \tag{8}$$

The idea was to cool down both operational amplifiers with the same heat sink so once selecting the heat sink for the operational amplifiers, the main restriction was to find a heat sink with lower thermal resistance than 2.05 °C/W. Also the heat sink should be small enough, so it would not take too much room from the rack case. The use of a LA 9/200 24V heat sink from Fischer Elektroniks was decided. It is a fan cooled heat sink exceeding the needed thermal resistance by more than a factor of ten with thermal resistance of 0.14°C/W so it is enough for cooling down two operational amplifiers attached onto it.

The heat sink was modified for the amplifiers. The top of the heat sink was partially cut and thinned so that the operational amplifiers could be installed there so that the amplifier chip has a good thermal path to the heat sink. The modified heat sink can be seen in figure 9.

**Figure 9.** LA 9/200 24V heat sink. One can see from the left hand side the shape that was cut for the ADA4870 evaluation boards. Also threaded holes were added for fixings. On the right one evaluation board is attached onto the heat sink. On the right end of the heat sink is seen the fan that blows air through the heat sink.

### 3.1.2 ADA4870 supply voltage sources

The ADA4870 amplifier requires -20 V and +20 V DC supply voltages for operation. These are provided by a pair of XP Power LCE80PS20 80 W power supplies with output current limit of 4.00 A [30]. The output currents of the supplies are monitored with ACS712 current sensors seen in figure 10. The operational amplifier consumes the least amount of power when the LC circuit is driven at its resonant frequency [19]. Thus, the sensed currents in the supplies for the operational amplifiers provide valuable information about the state of the LC circuit. With the help of these current sensors the amplifier can be shut down if too high current is sensed due to LC circuit being off resonance. This protects the sensitive ADA4870 operational amplifier from overheating and even from breaking.

The sensor gives out voltage signal that is linearly dependent on the sensed current as seen from figure 11. The current is monitored from each positive and each negative inputs for the operational amplifiers.

**Figure 10.** The ACS 712 current sensor used in monitoring the supply currents for the ADA4870 operational amplifiers. The supply voltage of 5 V DC is connected to the left and right side pins where the output signal is got from the central pin. The output signal is delivered through the rack case into the Wago$^{TM}$ I/O system for digitization. Figure from [31].

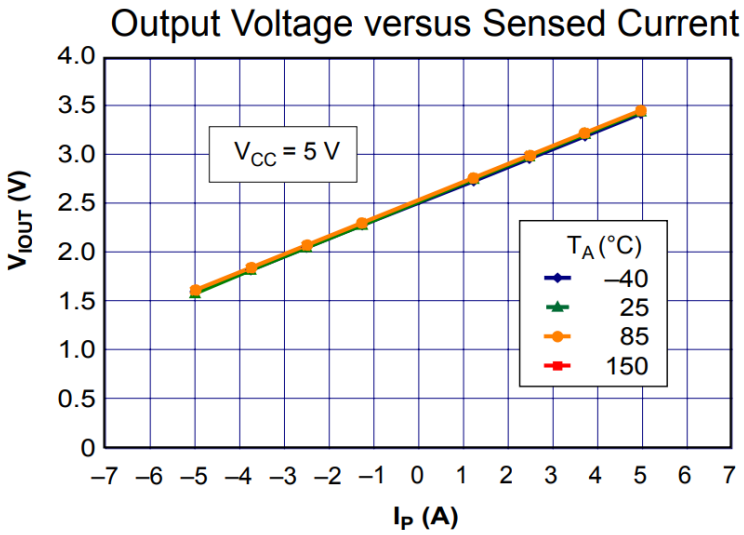


**Figure 11.** The output voltage of the ACS712 current sensor as a function of the sensed current. 2.5 V output voltage corresponds to no current flowing through the sensor. The currents in the supplies of the operational amplifiers should not exceed 1 A. This sets the lower limit for the - 20 V power supply to be around 2.4 volts and similarly upper limit of 2.6 volts for the + 20 V power supply. Figure from [32].

## 3.2 Transformer

### 3.2.1 Inductance of a coil

As described in section 1.3.1, the design goal frequency range for the amplifier was 500 - 1000 kHz. Since the capacitive load of the electrodes (which was estimated to be about 2-3 nF) cannot be avoided, there is an upper limit of the frequency range dictated by the fixed inductance value of the coil. To have the resonant frequency up to 1000 kHz, from equation (5) the inductance of the coil is required to be

$$\begin{aligned} L &= \frac{1}{4\pi^2 f_r^2 C} \\ &= \frac{1}{4\pi^2 \cdot 1000\text{kHz}^2 \cdot 2\text{nF}} \\ &= 0.00001267 \text{ H} \\ &\approx 13 \ \mu\text{H}. \end{aligned} \tag{9}$$

The choice of the inductance to be approximately 13 $\mu$H is also seen from figure

12. It shows the resonant frequency as a function of the capacitance with different values of inductance. One can see that the 13 $\mu$H line covers the wanted frequency range (500 kHz - 1000 kHz). The resonance is at 1000 kHz without any added capacitance on top of the cooler-buncher electrodes and the 500 kHz is reached with total capacitance of 7.4 nF.

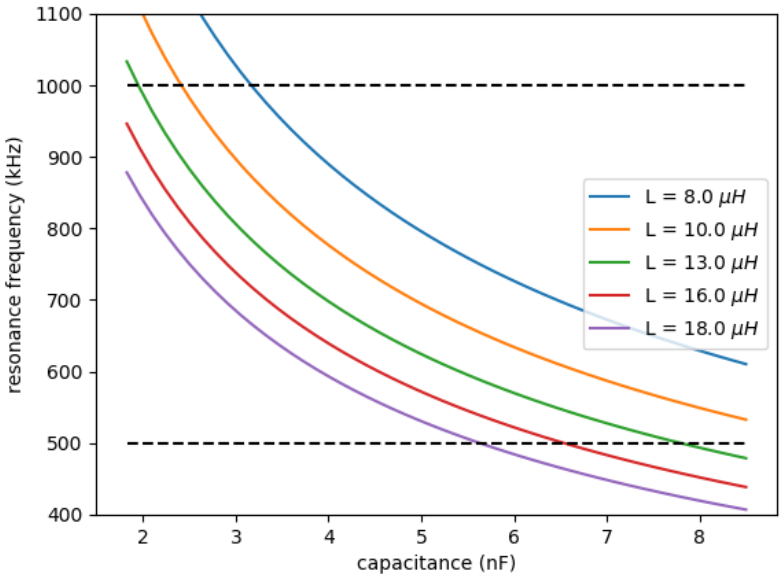


**Figure 12.** resonant frequency as a function of capacitance with several different values of inductance. It is seen that 13 $\mu$H is the best option for the inductance of a coil since it covers the most suitable frequency range (500 - 1000 kHz) marked with dashed lines. The resonance is at 1000 kHz without any added capacitance to the circuit.

### 3.2.2 Constructing the transformer

The inductance of a toroidal coil is [33]

$$L \approx \frac{\mu_0 \mu_r N^2 A}{2\pi r}, \tag{10}$$

where $\mu_0$ is the permeability of vacuum, $\mu_r$ is the relative permeability of the core material, $N$ is the number of turns around the core. $A$ is a cross-section area of a core and $r$ is the core radius measured from the center of the transformer to the center of the actual core material. This is illustrated in figure 13. From the equation (10) we see that the inductance is dependent on the geometry and material of the core as well as the number of turns of the conductor wire. By using the coil

as a transformer one can step up the voltage between the primary and secondary circuits. Ideally, the voltage amplification in a transformer is dependent on a ratio of the number of turns in primary and secondary side of a transformer as seen from equation (11).

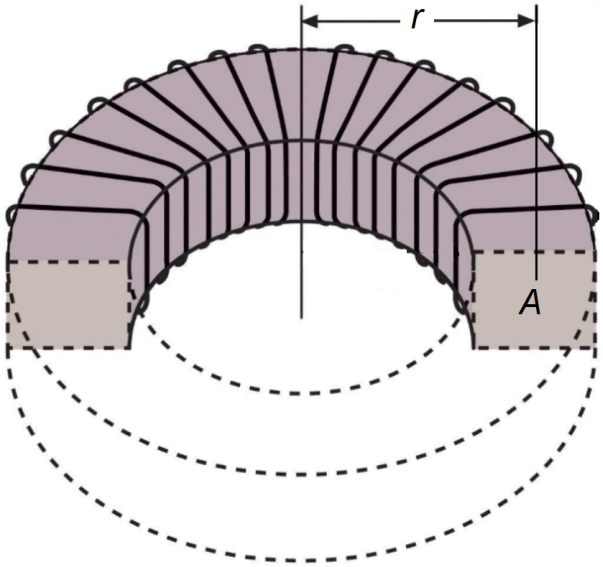


**Figure 13.** The geometry of the toroidal core used in this work. $A$ is a cross-sectional area of a core and $r$ is the core radius measured from the center of the transformer to the center of the actual core material. Figure from [34], modified.

$$\frac{V_1}{V_2} = \frac{N_1}{N_2}. \tag{11}$$

As seen from figure 8, the signal is first amplified through the operational amplifier before getting into the transformer. The maximum of 40 $V_{pp}$ as mentioned in section 3.1 is then driven through the primary side of the transformer. For this thesis work, the design goal amplitude is 400 $V_{pp}$ so the voltage gain in the transformer should be at least 10. This means that the number of turns in the secondary side needs to be at least 10 times more than in the primary side of the transformer while the calculated inductance of 13 $\mu$H is achieved.

As seen from equation (9), the wanted inductance of the coil can be achieved with several combinations of parameters $\mu_r$, $N$, $A$, and $r$. First, the physical size of the core was decided. Coil should be large enough so winding it can be done without special tools and small enough so it would not take too much room in the rack case. The decided size was a toroidal coil with outer diameter of 61 mm, height of 12.7

mm and cross sectional area of 1.58 $cm^2$

Different toroidal cores with relative permeability values between 1 and 40 were tested. The one with $\mu_r = 1$ was a 3D-printed air core. With low permeability, the wanted inductance of 13 $\mu$H requires more turns around the core as seen from equation (9). This will also lead to a greater voltage amplification in a transformer as seen from equation (11). On the other hand the increasing length of the wire will also increase the resistance of the coil. Testing the air core as a transformer did not give the wanted results. The signal was not delivered through the amplifier properly and thus the voltage amplification was not enough.

The coils using cores with higher relative permeability values worked better in the testing resulting in a greater voltage amplification through the transformer. The core material with a relative permeability of $\mu_r = 16$ was selected.

After fixing the dimensions and the core material type one could calculate the number of turns in the secondary side of the transformer to match the 13 $\mu$H inductance. From equation (9) the calculated number of turns for the $\mu_r = 16$ material is about 38.

The primary side of the transformer was wired with only one turn and measured its inductance to be 0.47 $\mu$H. The secondary side was wired so that the inductance will be 13 $\mu$H. This was achieved with 27 turns when measured inductance was 13.7 $\mu$H. The inductance was measured with LCR45 meter from Peak Electronic Design Ltd [35]. The winding differs from the expected number of turns by 29 % but the ratio 27/1 with the winding is enough as previously presented to provide the necessary voltage gain.

The holders for the transformers were designed so that they would be easy to install into the rack case and the wires should not move since the inductance of the coil is easily affected. The holders were then 3D-printed and they are seen in figure 14.

The operation of the transformer is also determined by so called skin effect in the wires. The skin effect causes the current density in the conductor to be largest near the surface of the conductor in the alternating current circuits. The skin effect is frequency dependent i.e. the higher the frequency of the current, the closer to the surface of the conductor the current will flow. This will reduce the effective cross section of the conductor and thus increase its effective resistance.

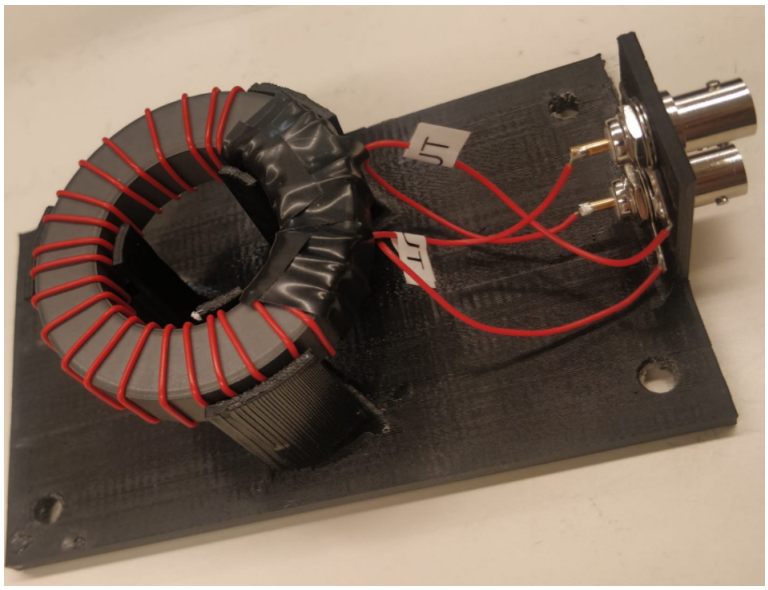

**Figure 14.** The 3D-printed holder for the transformer. The primary side has 1 turn and the secondary side has 27 turns of conductor wire. Both sides are connected to the BNC cables through BNC adapters seen on the right. The holes on the platform are for the installation of the holder to the rack case.

## 3.3 Tuning Capacitors

As seen from figure 8 the secondary side of the amplifier circuit is formed with the secondary side of the transformer coil and the cooler-buncher electrodes, which show up as a capacitive load. Just with this configuration, the circuit resonates at 1000 kHz frequency. To tune the resonant frequency to lower frequencies, additional tuning capacitors are used.

Having inductance of 13.7 $\mu$H, the lower limit of the frequency range (500 kHz) can be obtained by the capacitance of

$$\begin{aligned} C &= \frac{1}{4\pi^2 f_r^2 L} \\ &= \frac{1}{4\pi^2 \cdot 500\text{kHz}^2 \cdot 13.7\mu\text{H}} \\ &= 7.3957\text{nF} \\ &\approx 7.4\text{nF}. \end{aligned} \tag{12}$$

This means that in addition to the base capacitance maximum additional capacitance of 4.5 nF is required. This is achieved with two fixed 1.5 nF capacitors and

one variable capacitor (31 pF - 1558 pF), which gives the fine tuning possibility for setting the resonant frequency.

### 3.3.1 Fixed-value capacitors

For the fixed value capacitors the 1.5 nF Vishay Ceramic capacitors with voltage rating of 2 kV were used. Real capacitors have always some self-inductance which will occur at higher frequencies. On the other hand, the impedance of the capacitors usually decrease with increasing frequency [36]. These fixed value capacitors were connected in parallel to each other and separated from the circuit with small hand-usable switches. With these switches one can connect and disconnect the capacitors to be part of the LC circuit. The capacitors and the switches were assembled in a box seen in figure 15.

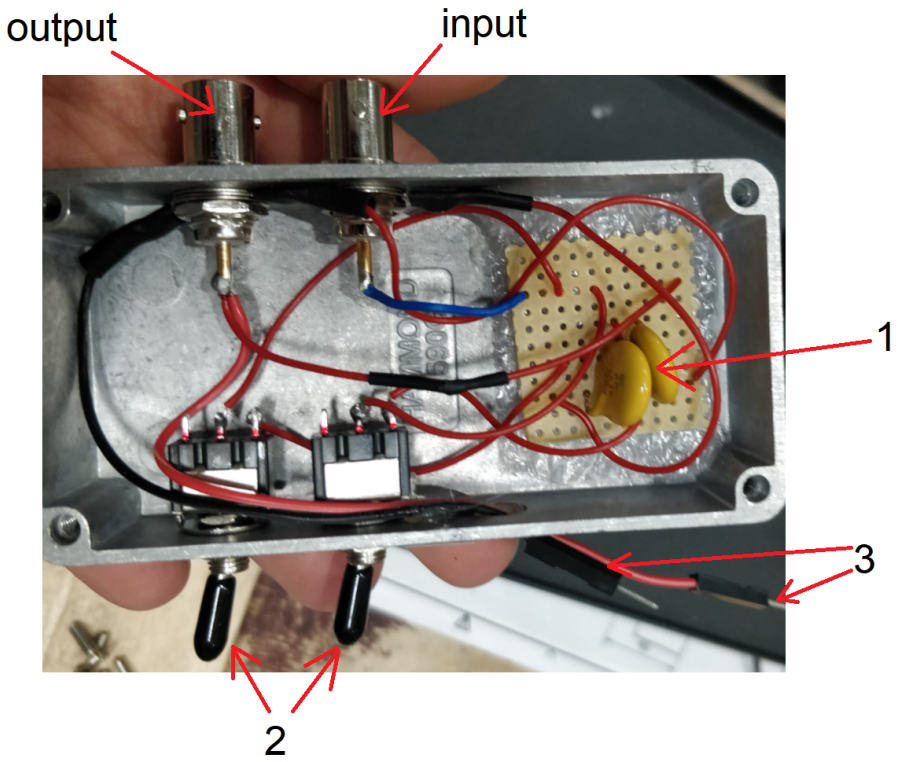


**Figure 15.** Fixed capacitor box for the y-side of the circuit. Capacitors of 1.5 nF can be seen in yellow (1). The manual flip-switches that connect and disconnect them into the circuit are seen on the bottom (2) and the connectors to the variable capacitor can be seen on the bottom right (3). Input and output of the box are through the BNC adapters on the top. Similar box was assembled to the x-side of the circuit as well.

### 3.3.2 Variable capacitors

The use of variable capacitors makes it possible to cover the whole desired frequency range without leaving any resonant frequencies unachievable. As previously mentioned in chapter 3.3, the additional 4.5 nF capacitance is needed for both x- and y-circuits to reach the lower end of 500 kHz resonant frequency. After addition of two fixed-value capacitors with capacitance of 1.5 nF each, the capacitance of 1.5 nF is still required. This is added by a variable capacitor 73-1-32-99N by Oren Elliott Products. It is a variable air capacitor with adjustable capacitance between 31 pF and 1558 pF and is seen in figure 16. The air capacitors have low leakage current and dissipation factor while regaining good stability and high insulation resistance. The voltage limit of the capacitor is 3100 $V_{pp}$, which is sufficient for the design voltage range (maximum 400 $V_{pp}$). The capacitor size (*length* = 22 cm) is small enough to fit in a rack case and the long adjusting stick in figure 16 makes the capacitor safe to use by hand. The variable capacitor and the fixed capacitors are all connected in parallel in the LC circuit so the total capacitance of the circuit is calculated by summing up the capacitance together. Thus, the capacitance of the LC circuit is adjustable between the base capacitance of the cooler-buncher electrodes and 7.5 nF. This means that the whole frequency range of 500 kHz - 1000 kHz is covered.

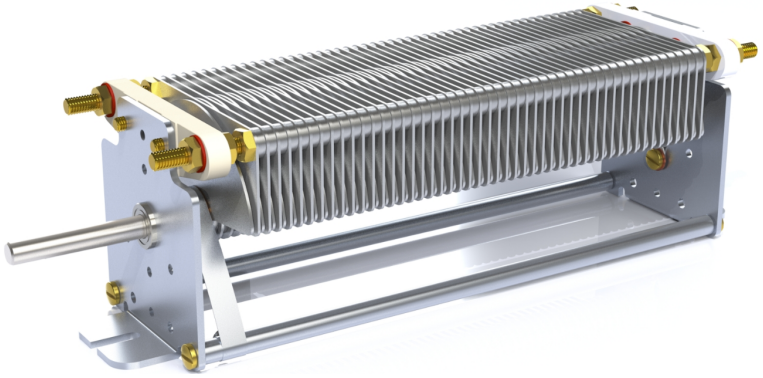

**Figure 16.** The 73-1-32-99N variable capacitor. The capacitance is adjustable between the range of 31 pF and 1558 pF by rotating the metal stick on the left. Figure from [37]

## 3.4 Assembling the amplifier

The amplifier was assembled into a rack case so the whole amplifier is a one single unit that can be easily moved and operated. The rack case was selected to be 19" Case RMCS190713BK1 by Hammond Manufacturing [38], which has dimensions of *width* = 432 mm, *depth* = 330 mm and *height* = 178 mm. The material of the rack case panels is aluminium that is painted with a nonconducting black paint. The parts were installed in the case so that the switches of fixed capacitors as well as the adjusting sticks for the variable capacitors were on the front side of the case. This allows one to operate them all easily from the same side. For the back side of the case a hole was cut for the heat sink air flow as well as the feedthrough for the power supplies. The feedthrough holes were also made for the input signals from the function generators and for the cable for monitoring the supply current flow of the operational amplifiers.

Every panel of the case was grounded as well as any parts inside not part of the circuits to make sure they were all at the same potential. This was verified by checking with a multimeter. The amplifier assembled in the rack case is seen in figures 17, 18 and 19.

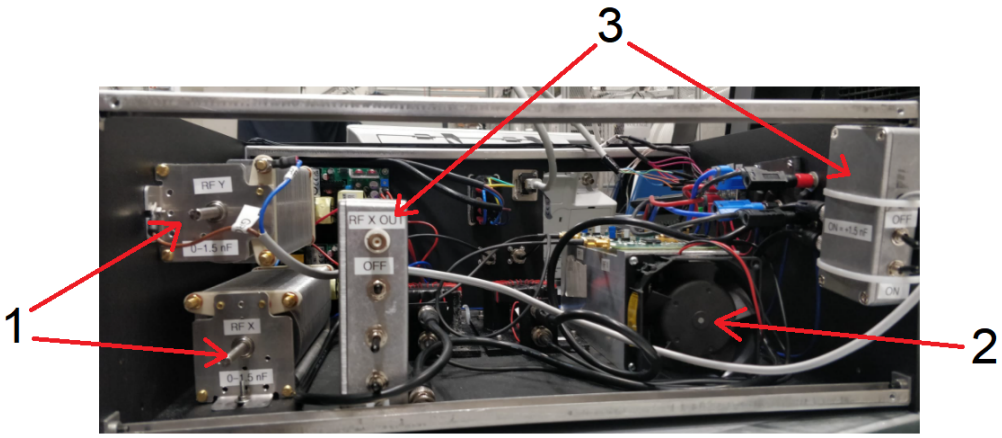


**Figure 17.** The front side of the amplifier case. On the left one can see the variable capacitors for both x- and y-sides of the circuit (1). On the right is the fan cooled heat sink, which blows air towards the back side of the case (2). The fixed-value capacitor boxes discussed in section 3.3.1 are also marked (3).

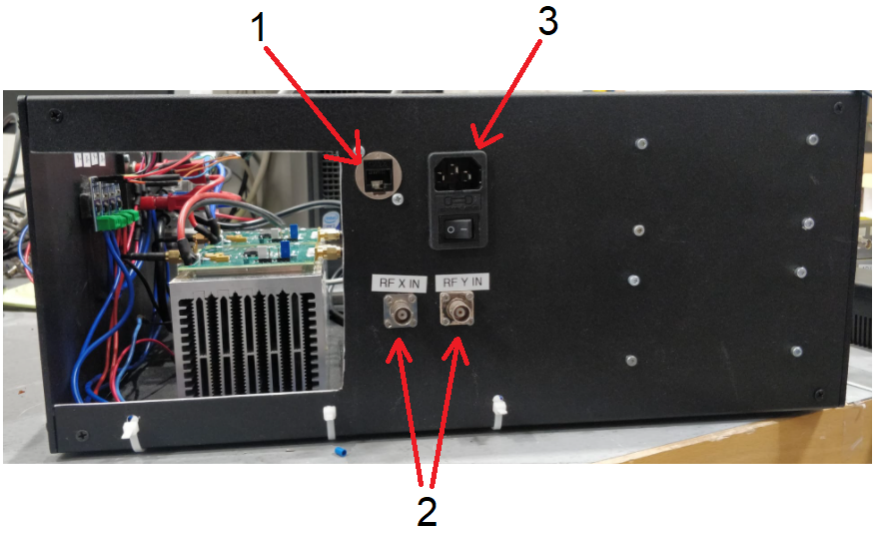


**Figure 18.** The back side of the amplifier case. On the left is the hole cut for the heat sink air flow out of the case. In the middle are the feedthroughs for the current monitoring (1), input signals from function generators (2) and a socket for 230 V AC to provide power to the DC supplies inside the case (3).

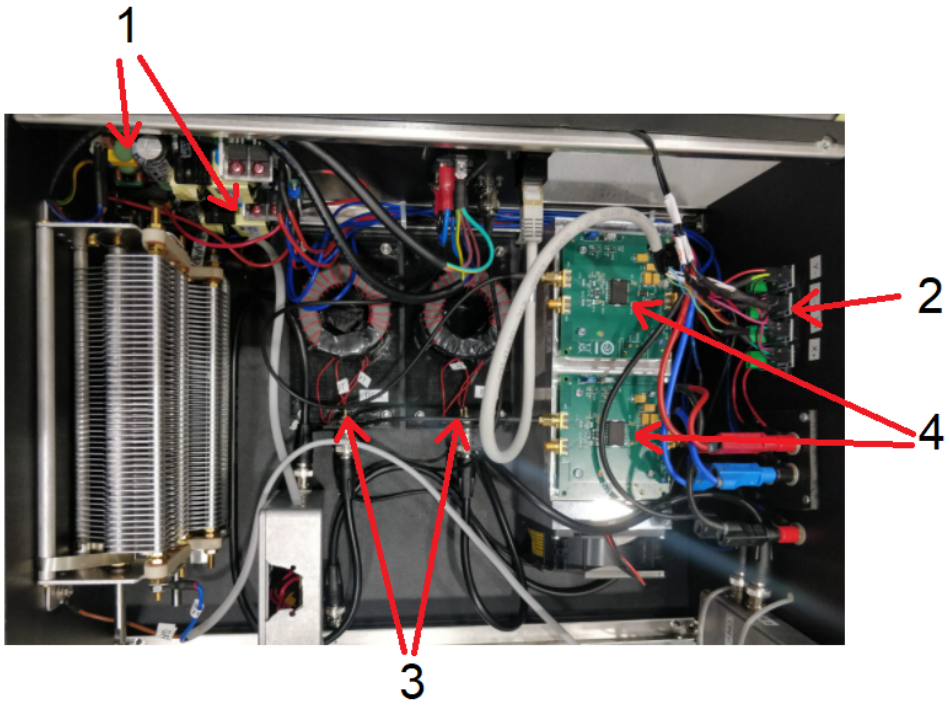


**Figure 19.** The top view of the amplifier case. The two power supplies offering $\pm 20$ V for the both side driver amplifiers are seen on the upper left (1) and the current sensors for these supplies on the right (2). In the middle are seen the transformers for both x- and y-sides of the circuit (3). Also the operational amplifiers attached onto the heat sink are marked (4).

# 4 Measurements and results

The $Q$ value represented earlier in section 2.1 indicates the quality of the LC circuit driven at the resonant frequency. The higher the $Q$ value, i.e., the smaller the bandwidth, the more ideally the circuit functions at the resonance. This leads to a higher voltage amplification gain with smaller power consumption. The $Q$ value can be calculated from the measurements as following [19]

$$\text{quality factor } Q = \frac{\text{resonant frequency}}{\text{bandwidth}} = \frac{f_0}{B} \tag{13}$$

where bandwidth is defined as the frequency range between the points where the voltage gain of the circuit falls to $1/\sqrt{2} \approx 0.71$ fraction of its resonance value [19]. The $Q$ factor of the circuit was modelled using LTspice simulation software as well as carrying out measurements with both simulated and actual load of the cooler-buncher electrodes. First the amplifier was tested and optimized by attaching it to a capacitive load using additional capacitors to mimic the real capacitance of the cooler-buncher electrodes. Finally, measurements were carried out by driving the amplified RF signal to the electrodes of the actual IGISOL cooler-buncher presented in section 1.3. The $Q$ factor is determined with different resonant frequencies from 600 kHz to 1 MHz with 50 kHz steps. Also the power consumption of the operational amplifiers was monitored during the measurements.

## 4.1 Simulations

The circuit of the RF amplifier was simulated using LTspice XVII software program. The simulated circuit is seen in figure 20.

The simulations were run with the LTspice XVII software with different input frequencies of the RF generator. The simulation was carried out by setting the LC circuit on resonance by tuning the capacitance of the circuit with additional capacitors. The frequency of the circuit was scanned from 20 kHz below to 20 kHz over the resonant frequency with 1 kHz steps. Then the capacitance was changed and the frequency of the circuit was run again across the resonance. The amplitude

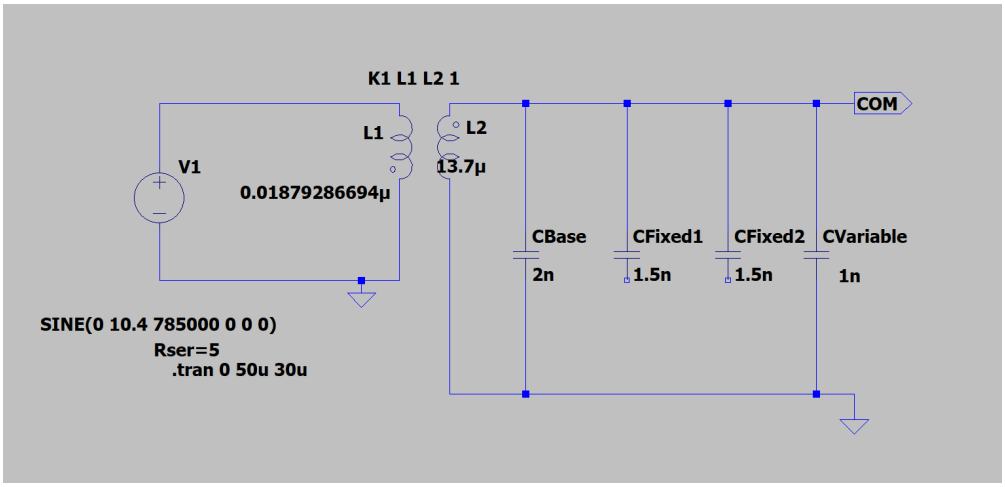


**Figure 20.** The circuit used to simulate the amplifier in LTspice XVII software. On the left is the primary circuit simulating the operational amplifier and primary side of the transformer. On the right is the secondary side of the circuit where the resonant frequency is changed with fixed capacitors and a variable capacitor. `CBase` simulates the capacitance of the cooler-buncher electrodes and `CFixed` capacitors are the fixed capacitors introduced in section 3.3.1 that can be connected and disconnected in the circuit. `CVariable` represents the adjustable capacitor, described in section 3.3.2, that is adjustable between 31 pF and 1558 pF.

of the LC circuit was monitored and plotted as a function of frequency. Example of this can be seen in figure 21.

For $Q$ factor determination, Gaussian function with a constant background $a \cdot e^{-(x-b)^2/(2 \cdot c^2)} + d$ was fitted in the data set. This function fitted best to the points near the peak of the resonance which is critical for $Q$ factor determination but is not valid approximation of the amplitudes below the constant parameter $d$. The example of the fitting can be seen in figure 21

After fitting the function, the $Q$ factor of the circuit can be calculated with equation (13) by searching the top of the fitted function and calculating the frequency range where the voltage is dropped to $1/\sqrt{2}$ of its highest value. From fitting in figure 21 the resonant frequency is 649.3 kHz and the bandwidth is 24.6 kHz. This means the $Q$ factor of the LC circuit for 650 kHz resonant frequency by simulation is

$$Q = \frac{f_0}{B} = \frac{649.3\text{kHz}}{24.6\text{kHz}} = 26.38 \approx 26. \tag{14}$$

The $Q$ factors for the other resonant frequencies were calculated similarly and the results can be seen in table 1 and in figure 22.

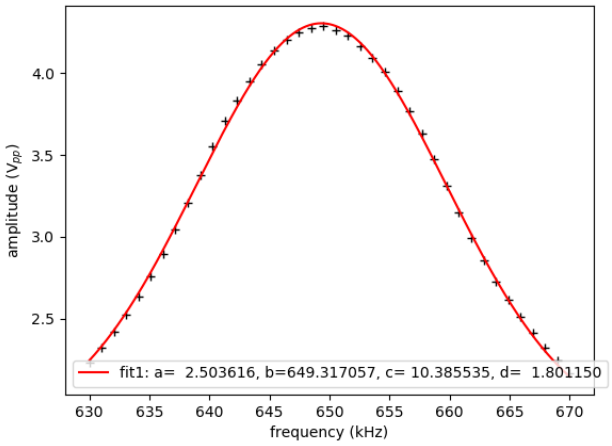


**Figure 21.** LTspice XVII software simulation of the circuit from figure 20. The capacitance of the LC circuit was matched to an analytically calculated resonant frequency of 650 kHz and the simulation was run from 630 kHz to 670 kHz. The exponential function is fitted for the $Q$ factor calculation.

**Table 1.** $Q$ factors for the LC circuit for different resonant frequencies obtained from the LTspiceXVII simulation. The resonant frequency of the circuit was tuned by changing the capacitance of the circuit with fixed-value and variable capacitors.

| resonant frequency | total capacitance | $Q$ factor |
|---|---|---|
| 600 kHz | 5.1 nF | 25 |
| 650 kHz | 4.4 nF | 26 |
| 700 kHz | 3.8 nF | 25 |
| 750 kHz | 3.3 nF | 25 |
| 800 kHz | 2.9 nF | 27 |
| 850 kHz | 2.6 nF | 28 |
| 900 kHz | 2.3 nF | 29 |
| 950 kHz | 2.0 nF | 27 |
| 1000 kHz | 1.8 nF | 29 |

The $Q$ factors for the LC circuit from simulations were between 25 and 29. The slight increase in the $Q$ factors as a function of resonant frequency is seen in table 1 and figure 22. The $Q$ factor of the circuit depends on the capacitance and inductance of the reactive components and is therefore dependent on the used components of the circuit.

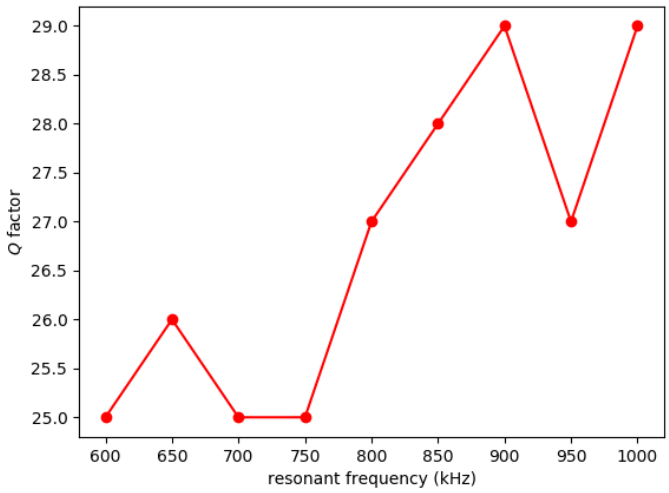


**Figure 22.** The $Q$ factors as a function of the resonant frequencies by the LTspice XVII simulations. One can see the slight frequency dependency of the $Q$ factor.

## 4.2 Measurements with a dummy load capacitance

Unfortunately, the cooler-buncher was nearly constantly used for measurements and was not available for this work. For this reason, one set of measurements, called "offline measurements", of the amplifier were done outside the actual cooler-buncher. This meant that the actual capacitance of the electrodes was not part of the circuit. This was replaced with an additional box of high voltage ceramic capacitors with a capacitance of 1500 pF for both x- and y-sides of the circuit. This additional capacitance was meant to act as the capacitance of the cooler-buncher electrodes and thus simulate the real load of the circuit as well as possible.

The measurements were done with the same resonant frequencies as the simulations above in section 4.1. The LC circuit was tuned into specific resonant frequencies with fixed and adjustable capacitors, see section 3.3.2, and the frequency of the input signal from function generator (Keysight 33500B [29]) was scanned from 20 kHz below resonance to 20 kHz over resonance with 1 kHz steps. The output amplitude for both x- and y-sides of the circuit were monitored with oscilloscope (Keysight DSOX3104A [39]) and plotted as a function of the input frequency. For $Q$ factor determination the function of a shape $a \cdot e^{-(x-b)^2/(2 \cdot c^2)} + d$ was fitted in the data sets as before in section 4.1. This can be seen in figure 23.

After fitting the functions, the $Q$ factor of the circuit can be calculated with equation (13) as before. The $Q$ factors and the amplitudes for offline measurements

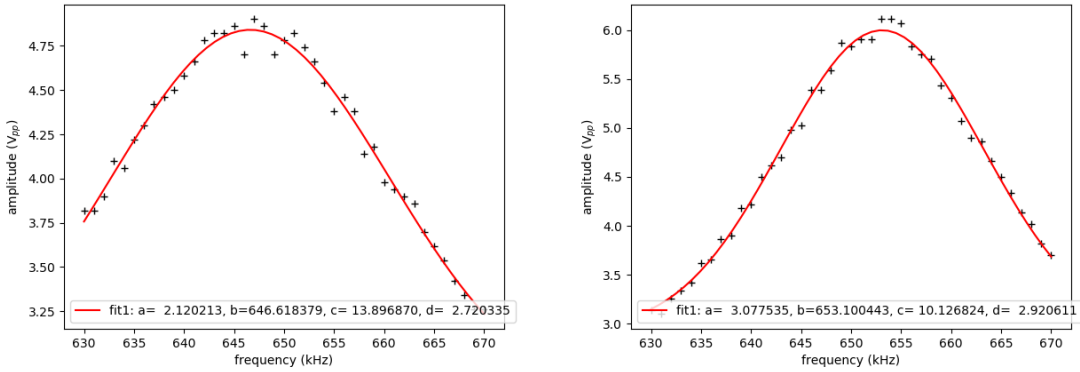


**(a)** Output amplitude as a function of frequency for the x-side of the circuit

**(b)** Output amplitude as a function of frequency for the y-side of the circuit

**Figure 23.** The fitted functions for the output amplitudes for x- and y-sides of the circuit when the resonance was tuned to the 650 kHz.

can be seen in table 2 and in figure 24.

**Table 2.** $Q$ factors and amplitudes for the LC circuit for different resonant frequencies by the offline measurements. Phase difference between x- and y-side were tuned to be 180 degrees. The input amplitude was kept at 0.1 $V_{pp}$ in order to protect the sensitive components of the circuit when off resonance.

| resonant frequency | $Q$ (x-side) | $Q$ (y-side) | Amp x ($V_{pp}$) | Amp y ($V_{pp}$) |
|---|---|---|---|---|
| 600 kHz | 19 | 23 | 5.3 | 5.3 |
| 650 kHz | 16 | 25 | 4.9 | 6.1 |
| 700 kHz | 15 | 25 | 4.9 | 6.4 |
| 750 kHz | 17 | 24 | 6.3 | 6.4 |
| 800 kHz | 15 | 20 | 5.5 | 5.6 |
| 850 kHz | 14 | 18 | 5.5 | 5.6 |
| 900 kHz | 12 | 18 | 5.5 | 5.6 |
| 950 kHz | 12 | 17 | 5.3 | 5.6 |
| 1000 kHz | 11 | 17 | 5.2 | 5.6 |

The $Q$ factors for the LC circuit by the offline measurements were between 11 and 25. These values are significantly lower than the values from LTspice simulation in section 4.1. The difference is probably due to additional resistance of the wires which is described by the skin effect, see section 3.2.2. In addition the resonant frequency was difficult to get precisely on the wanted frequency for both x- and y-sides of the circuit because their signals seemed to affect each other. This caused

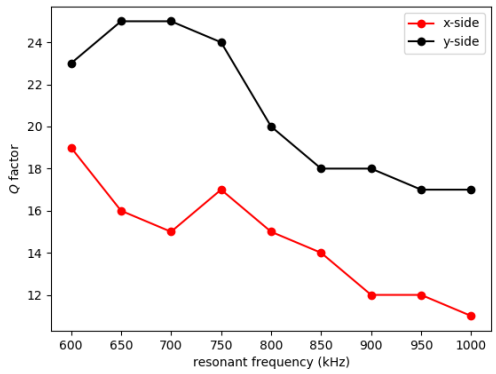


**(a)** The $Q$ factors as a function of the resonant frequencies.

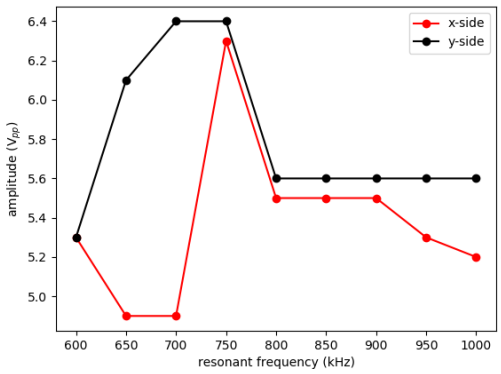


**(b)** The amplitudes as a function of the resonant frequencies.

**Figure 24.** The calculated $Q$ values and amplitudes for both x- and y-side circuits as a function of the resonant frequencies by the offline measurements.

the resonance to be more difficult to achieve for both sides simultaneously, which is why the resonance was determined by the frequency where the sum of the amplitudes was highest. The amplitude of the output signal varies significantly particularly with lower frequencies as seen from table 2 and figure 24b. The difference is mainly from the sensitive tuning of the resonant circuit. With manually adjustable capacitors the resonance was difficult to achieve simultaneously for x- and y-side circuits as mentioned before.

This cross-talk is visible in table 2 where the $Q$ factors for the x-side of the circuit are much lower than those for the y-side of the circuit. It is also noticeable that the $Q$ factors tend to be lower on higher frequencies on both x- and y-sides of the circuit. This frequency dependence of a $Q$ value is probably due to additional dummy load capacitance because it is no longer visible in the actual cooler-buncher measurements in section 4.3.

There are several factors affecting the accuracy of the offline measurements. The accuracy of the frequency ($\pm 1\mu$Hz) in figures 23 and 24 is determined by the function generator output accuracy [29]. The amplitude accuracy ($\pm$ 2.5 %) in figures 23 and 24b is determined by the oscilloscope used in measurements [39]. In fitting of the functions in figure 23 the fitting parameters $a$, $b$, $c$ and $d$ have errors which are negligible small in $Q$ factor calculation. For example the errors for the fitting parameters in figure 23a are $\delta a = 0.14, \delta b = 0.14, \delta c = 0.8$ and $\delta d = 0.15$ obtained from the curve fitting function [40].

In addition of the accuracy of the used measurement device, the used components affected the accuracy of the measurements. It was noticed for example that the winding of the coils was essential to be kept untouched since the moving of the wires affected the coil inductance and thus the resonant frequency of the circuit. Eventually the cross talking between the x- and y-side circuits was the biggest factor affecting the measurement. The signals from x- and y-side circuits clearly interfered with each other, which caused the high voltage amplitudes difficult to achieve simultaneously for both sides of the circuit.

## 4.3 Measurements with actual cooler-buncher electrodes

The online measurements of the amplifier were done attached to the cooler-buncher electrodes seen in figure 7. The signals for both x- and y-sides from the amplifier were attached into a DC box, where RF and DC signals are combined as mentioned in section 3. From the DC box these signals were attached to the both x- and y-side cooler-buncher electrodes. This meant that the actual capacitance of the electrodes as well as the resistance of the wires and DC box connectors were part of the circuit. The combined capacitance of these cooler-buncher electrodes was measured with LCR meter (LCR45 meter from Peak Electronic Design Ltd [35]) using test frequency of 200 kHz. The capacitance was measured to be around 1.7 nF relative to the ground for both x- and y-sides of the circuit. This differed 13 % of the simulated capacitance in measurements with a dummy load (1.5 nF). It was also detected that there was a notable cross-talk between x- and y-side circuits, which caused the induced signals to the electrodes even when that side amplifier circuit was switched off. This cross-talk is likely mostly due to vicinity of the x- and y-side electrodes to themselves but also the placement of the transformer and capacitors of x- and y-side in the constructed rack case likely have some cross-talk. The measurements were done simultaneously to the both x- and y-side electrodes. Due to the cross talking of the circuit the resonance was hard to achieve for both circuits simultaneously and the resonance was determined by the frequency where the sum of the amplitudes of x- and y-sides was highest. The problems with the connections caused that the lowest frequencies of 500 kHz and 550 kHz were unachievable in the actual measurements but the 600 kHz to 1000 kHz frequency range was covered and measured for both sides of the circuit.

For the $Q$ factor determination the function of a shape $a \cdot e^{-(x-b)^2/(2 \cdot c^2)} + d$ was fitted in the data sets as before in sections 4.1 and 4.2. This can be seen in figure 25. After fitting the functions, the $Q$ factor of the circuit was calculated with equation (13) as before in sections 4.1 and 4.2. The $Q$ factors for online measurements can be seen in table 3 and in figure 26

The $Q$ factors for the LC circuit by the online measurements were between 17 and 22. These values are significantly lower than the values from LTspice simulation in section 4.1 but are the same order of magnitude with offline measurements in section 4.2. This implies that the simulation load of the electrodes in the offline

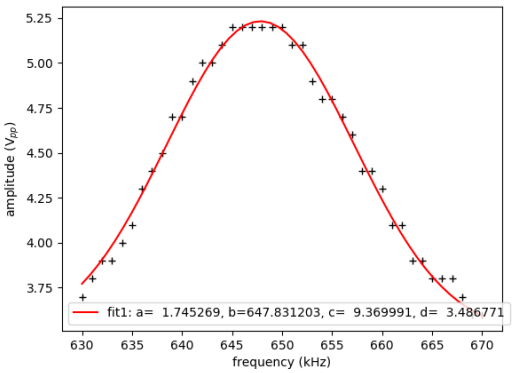


**(a)** Output amplitude as a function of frequency for the x-side of the circuit

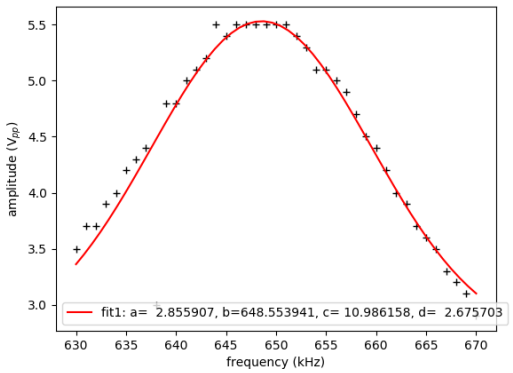


**(b)** Output amplitude as a function of frequency for the y-side of the circuit

**Figure 25.** The fitted functions for the output amplitudes for x- and y-side circuits when the resonance was tuned to the 650 kHz.

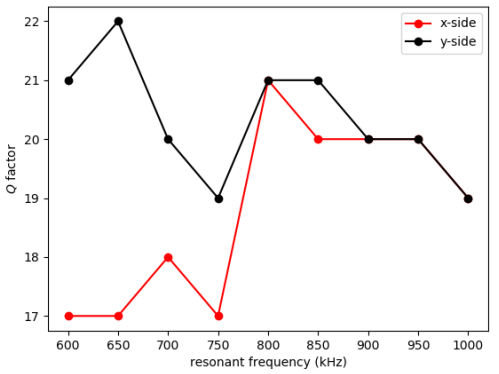


**(a)** The $Q$ factors as a function of the resonant frequencies.

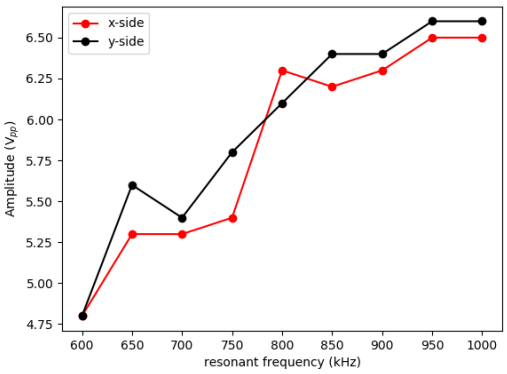


**(b)** The amplitudes as a function of the resonant frequencies.

**Figure 26.** The calculated $Q$ values and amplitudes for x- and y-side circuits as a function of the resonant frequencies by the online measurements.

**Table 3.** $Q$ factors and amplitudes for the LC circuit for different resonant frequencies by the online measurements. Phase difference between x- and y-side were tuned to be 180 degrees. The input amplitude was kept at 0.1 $V_{pp}$ in order to protect the sensitive components of the circuit when off resonance.

| resonant frequency | $Q$ (x-side) | $Q$ (y-side) | Amp x ($V_{pp}$) | Amp y ($V_{pp}$) |
|---|---|---|---|---|
| 600 kHz | 17 | 21 | 4.8 | 4.8 |
| 650 kHz | 17 | 22 | 5.3 | 5.6 |
| 700 kHz | 18 | 20 | 5.3 | 5.4 |
| 750 kHz | 17 | 19 | 5.4 | 5.8 |
| 800 kHz | 21 | 21 | 6.3 | 6.1 |
| 850 kHz | 20 | 21 | 6.2 | 6.4 |
| 900 kHz | 20 | 20 | 6.3 | 6.4 |
| 950 kHz | 20 | 20 | 6.5 | 6.6 |
| 1000 kHz | 19 | 19 | 6.5 | 6.6 |

measurements was quite good. In online measurements the $Q$ factors for the x- and y-sides of the circuit are better in line with each other than in the offline measurements. It is also noticeable that the $Q$ factors have weaker dependency on resonant frequency than in the offline measurements. The amplitudes and thus the voltage gain of the amplifier seem to increase with higher frequencies, this is seen from table 3 and from figure 26b. While increasing frequency, the $Q$ values stay stable which means that the bandwidth of the peak widens, this is seen from equation (13). The wider bandwidth of the voltage peak makes it easier to tune the circuit into the resonance which increases the amplification of the circuit.

The accuracy of the online measurements consists mainly on the same factors (same used measurement device and components of the circuits) than in the offline measurements, see section 4.2. The only difference is the change from the dummy load to the actual load of the cooler-buncher electrodes. The position of the cooler-buncher electrodes cannot be modified and this means that the cross talking between x- and y-side circuits cannot be totally avoided. This cross talking caused the same problems as in the offline measurements. The signals interfered with each other which caused the simultaneous voltage peak difficult to achieve for both circuits. This is seen in figure 25 where there is a slight frequency difference between the voltage peak positions. The cross-talk caused also the highest voltage values to be unachievable which is seen as a flat topness in figure 25. Once the x-side circuit closes its resonant

frequency the y-side circuit is still slightly off-resonance which burdens the x-side circuit causing it not to achieve its highest amplitude values. The same happens vice versa when the y-side circuit closes its resonant frequency. This happens because of the relative capacitance changes between x- and y-side electrodes. For example when the amplitude of the x-side increases, it changes the electric field experienced by the y-side electrodes which in turn changes the tuning of the resonance.

## 4.4 Power consumption

In offline and online measurements in sections 4.2 and 4.3 also the current consumption of the operational amplifiers of the circuits was monitored with the current sensors described in section 3.1.2. The power consumption of the operational amplifiers is obtained by multiplying the current consumption (accuracy of ± 0.5 %, [32]) with a supply voltage of 20V (accuracy of ± 0.5 %, [30]). The power consumption of the both x- and y-side amplifiers remained quite constant in all of the measurements with different resonant frequencies and the values were quite low (below 2 W).

The LC circuit should burden the operational amplifier least when in resonance and thus the power consumption of the operational amplifiers should be in minimum when the secondary circuit is in the resonance [19]. In the measurements, the input signal amplitude was kept only at 0.1 $V_{pp}$ because the circuit was driven off resonance on purpose: this small amplitude of the input signal protected the sensitive parts of the circuit from overheating and therefore also the power consumption of the operational amplifiers remained quite stable.

Therefore, one measurement with resonant frequency of 650 kHz was carried with a higher input amplitude of 2 $V_{pp}$. The voltage amplitudes as well as power consumption of the operational amplifiers of this measurement are seen in figure 27.

With higher input amplitude, the power consumption is clearly at the minimum at the resonant frequency. Although there is a slight difference in frequencies between the power minimum and amplitude maximum it is clear that the LC circuit consumes least amount of current and thus power when it is at the resonance. That is why keeping the circuit at the resonance during the use of the amplifier is extremely important since it protects the sensitive components of the circuit from overheating and breaking.

Ultimately, the amplifier was tuned into a testing resonant frequency of 850 kHz and the amplifier circuits were driven with higher input amplitudes, closer to the 10 $V_{pp}$ maximum output of the function generator, see section 3.1. The output amplitudes of 259 $V_{pp}$ were achieved with 4.50 $V_{pp}$ input signals for both x- and y-side circuits. The power consumption of the y-side driver amplifier was 7 W and 7.8 W, for the +20V and -20V power supplies, respectively. Similarly the power consumption of the x-side driver amplifier was 6 W and 5.6 W, for the +20V and -20V power supplies, respectively. The overall voltage gain of the amplifier seems to stay

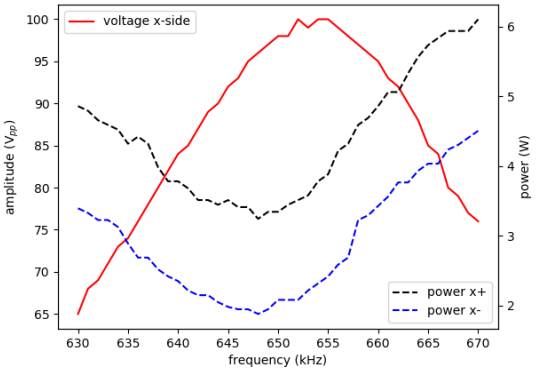


**(a)** Output amplitude and power consumption of the operational amplifier as a function of frequency for the x-side of the circuit

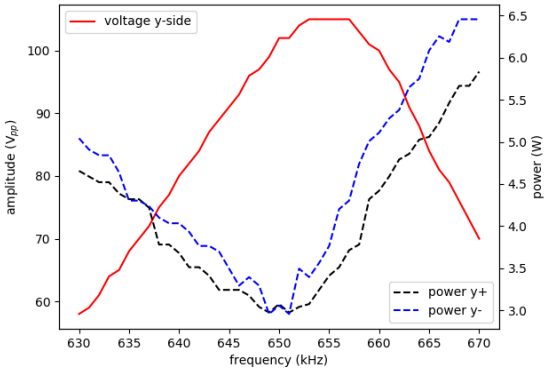


**(b)** Output amplitude and power consumption of the operational amplifier as a function of frequency for the y-side of the circuit

**Figure 27.** Output amplitudes and power consumption for x- and y-sides of the circuit with the resonant frequency of 650 kHz and an input amplitude of 2 $V_{pp}$. It is clearly visible that minimum power consumption also causes maximum output amplitude of the circuit.

around 60 in the measurements with both smaller input amplitude $\frac{V_{out}}{V_{in}} = \frac{6.3\text{V}}{0.1\text{V}} = 63$ and greater input amplitude $\frac{V_{out}}{V_{in}} = \frac{259\text{V}}{4.50\text{V}} = 58$.

# 5 Discussion

The RF amplifier was designed, simulated and constructed in order to improve the efficiency of the cooler-buncher used in the accelerator laboratory at the university of Jyväskylä. The objective was to achieve RF signal with 400 $V_{pp}$ of amplitude and an adjustable frequency range between 500 kHz and 1000 kHz. The measurements with the additional capacitors presenting the capacitive load of the electrodes seem to achieve these requirements, see section 4.2. In the measurements with the actual cooler-buncher electrodes, the cross talking between the x- and y-side circuit electrodes caused troubles in the signals, see section 4.3. The amplitude of 400 $V_{pp}$ was achieved with an input signal of 7 $V_{pp}$ but the frequency range was decreased to 600 kHZ - 1000 kHz. The cross talking between the electrodes of the cooler-buncher cannot be avoided since the electrodes need to be close to each other, see section 1.3.2. The cross talk could be minimized by moving the x- and y-side circuits and their conductors further apart from each other. With different design of the amplifier the frequency range could be widened down to 500 kHz.

One restrictive factor in this thesis was the use of a ferrite core material in the core of the transformer. This caused the inductance of the coils to increase rapidly with the amount of winding around the core, see equation (10). By changing the core material to aircore, one could get more winding around the core and thus more amplification through the transformer with the same fixed value of inductance (13.7 $\mu$H). This would increase the voltage gain and thus the achievable voltage range of the amplifier. On the other hand the increasing length of the wire in an aircore would also increase the resistance of the coil.

The $Q$ factors were calculated from the measurements with different resonant frequencies. The slight frequency dependency of the $Q$ factor is seen in numerical simulations in section 4.1 and in measurements with the additional capacitors presenting the capacitive load of the electrodes in section 4.2. However in the actual measurements with the cooler-buncher the frequency dependency is no longer noticeable.

The power consumption of the operational amplifiers is highly important since

the operational amplifier is the most sensitive part of the circuits and thus most vulnerable for overheating and breaking. It is shown in section 4.4 that the operational amplifiers consume the least amount of power when the LC circuits driven by them are kept in resonance. Thus, the adjustable resonant frequency of the LC circuits is critical. This is now achieved by manually tunable variable capacitors but in the future the changing of the resonant frequency could be achieved by programmable step motors which would speed up the tuning process as well as increasing the accuracy of the resonant frequency.

# References


[1] A. Nieminen et al. “Ion beam cooler-buncher at the IGISOL facility”. In: (2003). Ed. by J. Äystö et al. Pp. 429–429.

[2] A. Nieminen. “Manipulation of low-energy radioactive ion beams with an RFQ cooler; application to collinear laser spectroscopy”. In: (2002).

[3] J. Ärje et al. “Submillisecond On-Line Mass Separation of Nonvolatile Radioactive Elements: An Application of Charge Exchange and Thermalization Processes of Primary Recoil Ions in Helium”. In: *Phys. Rev. Lett.* 54 (2 Jan. 1985), pp. 99–101. DOI: 10.1103/PhysRevLett.54.99. URL: https://link.aps.org/doi/10.1103/PhysRevLett.54.99.

[4] M. Vilén. “Mass measurements and production of ions at IGISOL for the astrophysical r-and rp-processes”. In: *JYU dissertations* (2019).

[5] T. Eronen et al. “High-precision measurement of a low Q value for allowed -decay of 131I related to neutrino mass determination”. In: *Physics Letters B* 830 (2022), p. 137135. ISSN: 0370-2693. DOI: https://doi.org/10.1016/j.physletb.2022.137135. URL: https://www.sciencedirect.com/science/article/pii/S0370269322002696.

[6] J. Äystö. “Development and applications of the IGISOL technique”. In: *Nuclear Physics A* 693.1 (2001). Radioactive Nuclear Beams, pp. 477–494. ISSN: 0375-9474. DOI: https://doi.org/10.1016/S0375-9474(01)00923-X. URL: https://www.sciencedirect.com/science/article/pii/S037594740100923X.

[7] A. Nieminen et al. “Beam cooler for low-energy radioactive ions”. In: *Nuclear Instruments and Methods in Physics Research Section A: Accelerators, Spectrometers, Detectors and Associated Equipment* 469.2 (2001), pp. 244–253. ISSN: 0168-9002. DOI: https://doi.org/10.1016/S0168-9002(00)00750-6. URL: https://www.sciencedirect.com/science/article/pii/S0168900200007506.

[8] V. J. Virtanen. “Offline commissioning of the multi-reflection time-of-flight mass separator at JYFLTRAP”. In: (2019).

[9] T. Eronen. “Mass measurements of proton-rich nuclei with jyfltrap”. In: *Acta Physica Polonica B* 42.3-4 (2011). Cited by: 0, pp. 559–566. DOI: 10.5506/APhysPolB.42.559. URL: https://www.scopus.com/inward/record.uri?eid=2-s2.0-79953714875&doi=10.5506%2fAPhysPolB.42.559&partnerID=40&md5=c432fbff9835ed269e514a8f42edc406.

[10] S. Kujanpää. “Determination of the magnetic octupole moment of 173-Yb and a design towards laser-double resonance methods in an MR-ToF device”. In: (2020). Ed. by M.-l. tiedekunta et al.

[11] C. Delafosse et al. “First trap-assisted decay spectroscopy of the 81Ge ground state”. In: European Physical Journal A (2022).

[12] R. P. de Groote et al. “Magnetic octupole moment of 173Yb using collinear laser spectroscopy”. In: Physical Review A (2021). Ed. by F. laitos and D. of Physics.

[13] P. Delahaye et al. “The MORA project”. In: Hyperfine Interactions (2019). Ed. by F. laitos and D. of Physics.

[14] T. Brunner et al. “TITAN’s digital RFQ ion beam cooler and buncher, operation and performance”. In: *Nuclear Instruments and Methods in Physics Research, Section A: Accelerators, Spectrometers, Detectors and Associated Equipment* 676 (2012). Cited by: 70; All Open Access, Green Open Access, pp. 32–43. DOI: 10.1016/j.nima.2012.02.004. URL: https://www.scopus.com/inward/record.uri?eid=2-s2.0-84862807910&doi=10.1016%2fj.nima.2012.02.004&partnerID=40&md5=f7747bd931fa578ebad3ee253c1abf52.

[15] G. Araneda. “Experiments with single photons emitted by single atoms”. In: (Apr. 2019). DOI: 10.13140/RG.2.2.33220.17288.

[16] P. H. Dawson. “Quadrupole mass spectrometry and its applications”. In: (2013).

[17] S. Kahra. “Trapping and cooling of single molecular ions for time resolved experiments”. In: (Mar. 2011). URL: http://nbn-resolving.de/urn:nbn:de:bvb:19-128803.

[18] A. Reuben et al. “Ion trajectories in exactly determined quadrupole fields”. In: *International Journal of Mass Spectrometry and Ion Processes* 154.1 (1996), pp. 43–59. ISSN: 0168-1176. DOI: https://doi.org/10.1016/0168-1176(96)04374-1. URL: https://www.sciencedirect.com/science/article/pii/0168117696043741.

[19] N. Storey. “Electronics A Systems Approach”. In: (2013).

[20] M. Smith. “A square-wave-driven radiofrequency quadrupole cooler and buncher for TITAN”. In: Retrospective Theses and Dissertations, 1919-2007 (2005). DOI: http://dx.doi.org/10.14288/1.0085163. URL: https://open.library.ubc.ca/collections/ubctheses/831/items/1.0085163.

[21] M. Martin et al. “An RF amplifier for ICRF studies in the LAPD”. In: 1689.1 (2015), p. 070010.

[22] O. Nezhevenko et al. “Performance of X-band pulsed magnicon amplifier”. In: (2003), pp. 1128–1130.

[23] P. Beller et al. “The Frankfurt RF-driven ion source”. In: *Nuclear Instruments and Methods in Physics Research Section A: Accelerators, Spectrometers, Detectors and Associated Equipment* 449.1-2 (2000), pp. 16–21.

[24] P. A. Seidl et al. “Multi-beam RF accelerators for ion implantation”. In: (2018), pp. 184–187.

[25] H. G. Koenig et al. “The FAIR-SIS100 Bunch Compressor RF Station”. In: (), pp. 2759–2761. DOI: 10.18429/JACoW-IPAC2018-WEPML032. URL: http://accelconf.web.cern.ch/ipac2018/papers/WEPML032.pdf.

[26] *LPC Caen JF cam 05/2020.*

[27] *https://www.analog.com/media/en/technical-documentation/data-sheets/ada4870.pdf.*

[28] *https://www.analog.com/media/en/technical-documentation/user-guides/ADA4870ARR-EBZ-UG-685.pdf.*

[29] *https://www.keysight.com/us/en/assets/7018-05928/data-sheets/5992-2572.pdf.*

[30] *https://www.farnell.com/datasheets/3217096.pdf.*

[31] *https://create.arduino.cc/projecthub/instrumentation-system/acs712-current-sensor-87b4a6.*

[32] *https://www.sparkfun.com/datasheets/BreakoutBoards/0712.pdf.*

[33] *http://hyperphysics.phy-astr.gsu.edu/hbase/magnetic/indtor.html.*

[34] *https://owenduffy.net/blog/?p=18253.*

[35] *https://www.peakelec.co.uk/downloads/lcr45-datasheet-en.pdf.*

[36] *https://eepower.com/capacitor-guide/fundamentals/impedance-and-reactance.*

[37] *https://www.orenelliottproducts.com/product/73-1-32-99n/.*

[38] *https://www.hammfg.com/electronics/small-case/rack-mount/rmc.*

[39] *https://www.keysight.com/us/en/assets/7018-02734/data-sheets/5990-6619.pdf.*

[40] *https://docs.scipy.org/doc/scipy/reference/generated/scipy.optimize.curve$_f$it.html.*